Electrostatic diagnostics of nanosecond pulsed electron beams in a Malmberg–Penning trap

B. Paroli, G. Bettega, G. Maero, M. Romé, M. Norgia, A. Pesatori, and C. Svelto

---

Articles you may be interested in

Equilibrium of non-neutral plasmas in a Malmberg–Penning trap with quadrupole field errors
Phys. Plasmas **16**, 122103 (2009); 10.1063/1.3265966

Experimental and numerical analysis of the electron injection in a Malmberg-Penning trap
Phys. Plasmas **14**, 042104 (2007); 10.1063/1.2721072

Analysis of the electron injection in a Malmberg-Penning trap
AIP Conf. Proc. **862**, 128 (2006); 10.1063/1.2387917

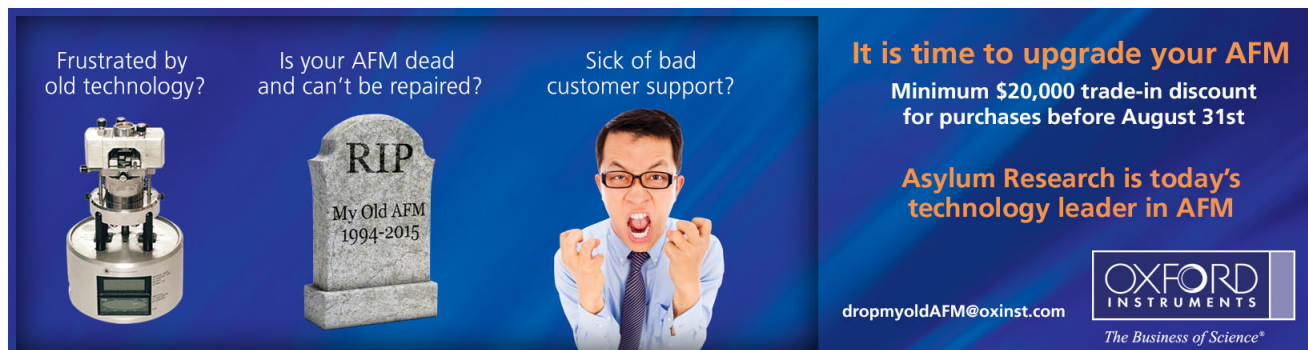Annular Malmberg–Penning trap for studies of plasma confinement
Rev. Sci. Instrum. **70**, 2993 (1999); 10.1063/1.1149860

Confinement of test particles in a Malmberg–Penning trap with a biased axial wire
Phys. Plasmas **4**, 1196 (1997); 10.1063/1.872299

Electrostatic diagnostics of nanosecond pulsed electron beams in a Malmberg–Penning trap

B. Paroli,[1,a)] G. Bettega,[1,b)] G. Maero,[1] M. Romé,[1] M. Norgia,[2] A. Pesatori,[2] and C. Svelto[2]

[1]*Dipartimento di Fisica and I.N.F.N. Sezione di Milano, Università degli Studi di Milano, Via Celoria 16, 20133 Milano, Italy*
[2]*Dipartimento di Elettronica e Informazione del Politecnico di Milano, Piazza Leonardo da Vinci 32, 20133 Milano, Italy*

A fast electrostatic diagnostic and analysis scheme on nanosecond pulsed beams in the keV energy range has been developed in the Malmberg–Penning trap ELTRAP. Low-noise electronics has been used for the detection of small induced current signals on the trap electrodes. A discrete wavelet-based procedure has been implemented for data postprocessing. The development of an effective electrostatic diagnostics together with proper data analysis techniques is of general interest in view of deducing the beam properties through comparison of the postprocessed data with the theoretically computed signal shape, which contains beam radius, length, and average density as fit parameters. © *2010 American Institute of Physics.* [doi:10.1063/1.3455200]

I. INTRODUCTION

The diagnostics and control of plasma collective effects have a fundamental importance when dealing with high-quality charged-particle beams. For instance, phenomena such as space-charge repulsion play a negative role in breaking the bunch spatial coherence.[1] Such effects can be of difficult investigation at high energies and short time scales. One can nevertheless take advantage of scaling laws governing the transversal dynamics[2,3] and obtain fruitful information from studies at much lower energies.[4] In this sense cylindrical Malmberg–Penning traps[5] can be beneficial. They are usually employed for the observation of collective phenomena in trapped single charged plasmas, but due to their versatility and ease of operation they are also suited to a beam configuration.

The Malmberg–Penning trap ELTRAP (Ref. 6) has already been used in the past in such a transmission mode for continuous, low-energy beams.[7] The apparatus has been recently upgraded with the aim of exploiting the Thomson backscattering technique as an additional tool for the diagnostics of bunched electron beams. The information obtained with this technique will complement the results of other diagnostic tools based on the analysis of electrostatic signals.

The device is sketched in Fig. 1. An electron bunch is produced by a photocathode source, illuminated by a UV laser (λ=337 nm) with a pulse of time duration $\leq$5 ns. The bunch energy is determined by the negative bias applied to the source with respect to the grounded cage, and can be varied in the range of 0.1–10 keV. The beam is shot through the trap, consisting of ten cylindrical electrodes of diameter 90 mm immersed in a homogeneous, longitudinally directed magnetic field of strength up to 0.2 T. Eight cylinders (C1–C8) have length of 9 cm, while two (S2 and S4) have length of 15 cm and are split into two and four azimuthal sectors, respectively. The beam finally impinges on a phosphor screen and the emitted light is recorded by a charge-coupled device camera.

In Ref. 8 we have used a destructive diagnostics technique to investigate the properties of the electron bunch, exploiting the phosphor screen both as imaging device and charge collector. There we have demonstrated that the axial length of the bunch depends not only on the duration of the laser pulse but also on the space-charge of the bunch itself which can lead to a significant spread. In the future the screen will be removed to implement the Thomson backscattering apparatus comprising an infrared (IR) laser and an array of photomultipliers. As an alternative to the charge collector and as a complement to the Thomson backscattering we propose here a fully nondestructive measurement based on the current signals induced on the trap electrodes by the crossing of the beam. The information can be used, for instance, for the synchronization of the electron bunch and the IR laser pulse.

In the following we shall briefly outline the theoretically expected shape of the signal and then evaluate the expected signal-to-noise ratio (SNR). We shall then describe the amplification system and the data postprocessing technique developed to disentangle the signal from the noise. The residual distortion observed in the final results is then discussed through an accurate characterization of the transmission line and first relevant physical information on the beam properties is presented. Finally, we summarize the results and give an outlook on future work.

II. SIGNAL FORMATION AND SNR

The image current induced on a cylindrical antenna (i.e., one of the trap electrodes) by a finite-size electron pulse can

---

a)Also at: Politecnico di Milano, Piazza Leonardo da Vinci 32, 20133 Milano, Italy.
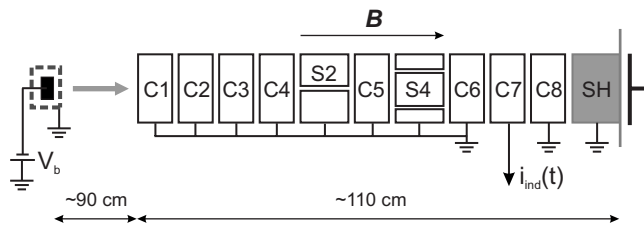b)Present address: Via Piave 7, 23824 Dorio, Italy.

FIG. 1. Sketch of the ELTRAP apparatus in transmission mode (not to scale). The electron bunch comes from the photocathode on the left with an energy set by the bias voltage V_b and travels along the axis of the trap up to the planar charge collector. The trap itself consists of ten cylindrical electrodes (C1–C8 plus S2 and S4, azimuthally two- and fourfold split, respectively) and a permanently grounded shield SH (in gray). An axial magnetic field (up to $B=0.2$ T) provides radial focusing of the beam. In the present experiments the C7 electrode has been used as antenna.

FIG. 3. (a) Comparison of calculated induced signal and measured background noise. The induced signal is shown as voltage drop across a load impedance of $Z=50$ Ω. (b) Noise signal on the C7 electrode, measured with a digital oscilloscope (1 kS, 5 GS/s) and input coupling of 50 Ω. Notice the different time scales on the horizontal axis.

be obtained using the Ramo theorem.[9] The schematic is shown in Fig. 2. A cylindrical (r,θ,z) coordinate system is adopted. The pick-up electrode has axial length L_A, radius R_W, and is enclosed within two ideally infinitely long, grounded conducting cylinders. A bunch with radius R_B, length L_B, and uniform particle density n is assumed. The motion of the bunch is considered assigned through the coordinates of its center $[r_C(t),\theta_C(t),z_C(t)]$, approaching the antenna from $z=-\infty$ with constant axial velocity v_C. Then the induced current signal on the antenna reads

$$i_{\text{ind}}(t) = 4env_C \int_0^{2\pi} d\theta \int_0^{R_B} r'\,dr' \int_{-L_B/2}^{L_B/2} dz' \int_0^{\infty} dk_z \sin(\pi k_z L_A)$$

$$\times \frac{I_0(2\pi k_z \tilde{r})}{I_0(2\pi k_z R_W)} \sin[2\pi k_z(z_C + z')], \tag{1}$$

where $\tilde{r}=\sqrt{r'^2+r_C^2+2r'r_C\cos\theta}$, $-e$ is the electron charge, and $I_0(r)$ is the zeroth order modified Bessel function.

Figure 3 shows an example of the induced signal obtained using typical experimental values: $n\approx 10^{12}$ m^{-3}, bunch energy $E=2$ keV, radius $R_B=3$ mm, and length $L_B=10$ cm. Figure 3(a) shows a voltage signal obtained as $V_{\text{ind}}(t)=Zi_{\text{ind}}(t)$, as if the antenna was connected to a load impedance of $Z=50$ Ω through an ideal transmission line. In this way we can compare the expected signal with the noise read at the output of the real transmission line shown in Fig. 3(b). The theoretical calculations indicate that the time width of the signal is 10 ns, therefore requiring an input bandwidth larger than 100 MHz. The estimated peak value is less than 2 mV and by comparison with the measured background noise we expect to work in poor SNR conditions. It has been experimentally verified that no induced signal is visible without
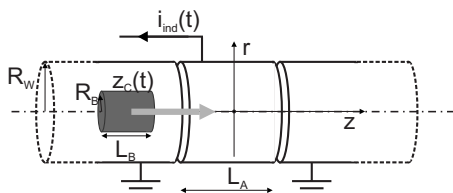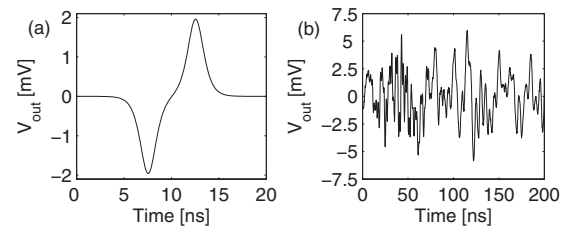
amplification when directly connecting the output of the transmission line to a digital oscilloscope fulfilling the analogical band request.

III. SIGNAL AMPLIFICATION

The fundamental issue of a poor SNR has been solved by designing a low-noise broadband transimpedance input stage. The circuit has been built using bipolar junction transistors BFR 540 in the SMD package. We have chosen the common-emitter–common-base (CE-CB) cascode configuration[10] shown in Fig. 4, a topology that has the great advantage of reducing the Miller input capacitance and therefore increasing the bandwidth. The network works as a transimpedance stage directly driven by the base current which comes from the antenna. The measured bandwidth (at -3 dB) is 180 MHz and the gain of the stage is 10^4 V/A. In order to achieve a higher signal level we have added to the output of the transimpedance stage a voltage amplifier (Miteq, Hauppauge, NY 11788, AU-1534) having 500 MHz bandwidth and 32 dB gain.

Since high energy bunches determine shorter signals with high induced current peaks we have connected the circuit to a 13 dB attenuator, in order to avoid the saturation occurring on the Miteq amplifier when the extraction voltage is higher than 7 kV. As an estimate, using the peak value of the computed current signal shown in Fig. 3(a) we expect after amplification a signal level of $V_{\text{out}}|_{\text{peak}} \approx 1.8$ [mV]/50 $\Omega \times 10^4$ [V/A]$\times 9$ [V/V]≈ 3.2 V, thus completely solving the problem of poor SNR. The last amplification factor of 9 [V/V] is the net effect of the Miteq amplifier and of the attenuator $(-13$ [dB]$+32$ [dB] $=19$ [dB]). Notice that the expected value was computed assuming a voltage drop over a 50 Ω impedance while the amplifier makes use of a $1-200$ Ω trimmer which is empirically adjusted to optimize the output. Experimental tests have shown that the voltage amplifier is able to reveal the current pulses through the amplification of the voltage drop across its input impedance. For instance, the device has been recently exploited[11] when measuring diocotron oscillations[12] in a trapped electron plasma at low density and temperature.

IV. WAVELET-BASED DATA ANALYSIS

During the experiments the measured noise [see Fig. 5(a)] forming on the transmission line increases in amplitude because of the disturbances introduced by the high voltage

FIG. 2. Two-dimensional model in (r,z) geometry for the calculation of the induced charge on a cylindrical pick-up. L_A is the axial length of the electrode, R_W its radius, while R_B and L_B are the dimensions of the electron bunch of center coordinates $[r_C(t),\theta_C(t),z_C(t)]$.
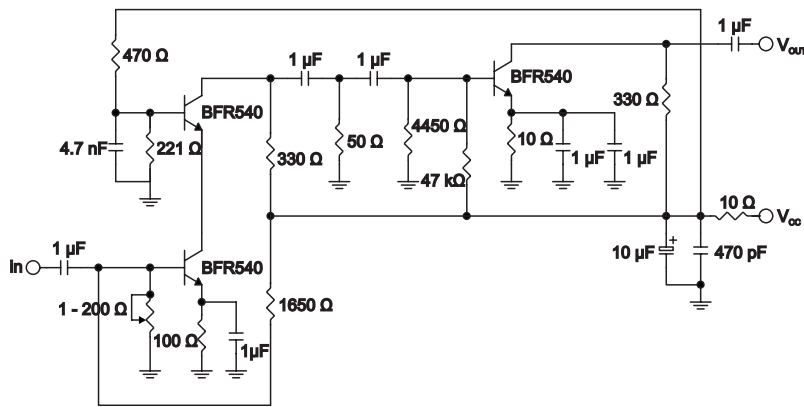
FIG. 4. Schematic of the input stage of the amplification circuit.

generators for the phosphor screen and photocathode biasing, and by the high current generator (up to 600 A) of the magnet coils.

Figure 5(a) shows the background noise without any signal from currents induced by the electron bunch as it appears at the output of the amplification system. The random component present along the whole record is increased by periodic noise bursts due to the electromagnetic disturbances caused by the plasma discharge inside the UV laser cartridge. This is apparent in the figure at $t=0$, when the laser is triggered. Notice that the measurement of this disturbance has been performed keeping the laser mechanical shutter closed so that the photocathode does not emit electrons, and by consequence the signal does not contain any induced charge contribution. Here data acquisition is triggered by the transistor-transistor logic synchronization signal coming from the laser device, indicating the presence of the laser output.

Since the noise contains both deterministic and random components, the signal in Fig. 5(a) cannot be directly subtracted from the raw data. Therefore we have disentangled the deterministic and stochastic components using the wavelet transform.[13] A noise record of 5000 samples at a sampling rate of 5 GS/s has been expanded into wavelet series. The Symlet8 wavelet has been used in the analysis due to the high number (7) of vanishing moments, allowing a perfect reconstruction, through the associated scaling functions, of polynomials up to the seventh order. After the decomposition, the noise signal has been filtered following Donoho's hard thresholding.[14,15] The optimal threshold value $\epsilon_T = \sigma\sqrt{2 \ln N}$ has been used, where N is the length of the signal and σ is its standard deviation. The signal has been reconstructed retaining the wavelet coefficients greater, in absolute value, than the threshold and applying the inverse wavelet transform. The result yields the deterministic disturbance due to the laser discharge [see Fig. 5(b)], while the discarded coefficients represent the uncorrelated noise, which is obtained by subtraction from the overall noise signal [see Fig. 5(c)]. The deterministic component, taken as zero level for each measurement, has been subtracted from the raw data. The resulting signals have been cleaned from the random noise with the same wavelet filter, i.e., a Symlet8 with hard thresholding. Figure 6 shows some signals taken at different electron bunch energies after the denoising routine.
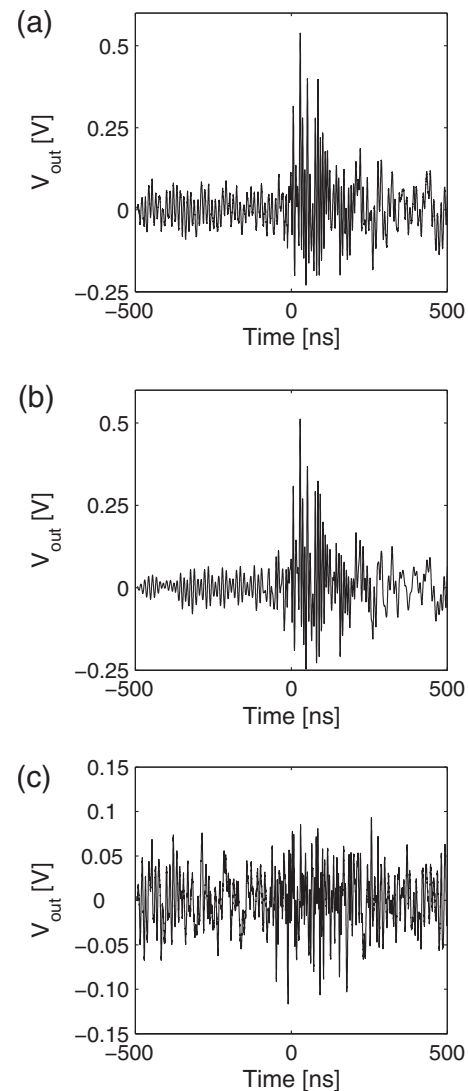

FIG. 5. Results of the wavelet filtering process on the noise signal. (a) The overall noise signal (5 kS acquired at 5 GS/s) is recorded operating the UV laser with closed shutter, i.e., in the absence of electron bunch emission. (b) The wavelet filter yields a fixed (deterministic) noise component due to the laser discharge. (c) By subtraction of the deterministic part, the statistical component of the noise is obtained. The time $t=0$ corresponds to the laser trigger.
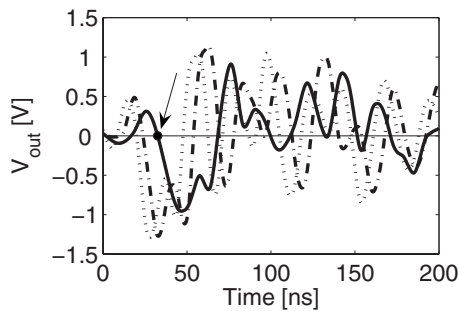
FIG. 6. Smooth signals from currents induced by an electron bunch in the pick-up electrode of the Malmberg–Penning trap. The noise-free curves were obtained with the wavelet-based denoising algorithm. The continuous, dashed-dotted, and dotted lines correspond to a photocathode source bias $V_b = -4, -7, -10$ kV, respectively. The arrow indicates the second zero crossing (used in Sec. VI for the estimate of the TOF) of the -4 kV signal.

V. CHARACTERIZATION OF THE TRANSMISSION LINE

Figure 6 shows that the measured signals are affected by oscillations. The reason for this behavior is attributed to impedance discontinuities in the transmission line, caused by the fact that the antenna is connected to the oscilloscope by a series of different conductors: the 18 Ω kapton-insulated wire from the electrode to the vacuum feedthrough, enclosed within the ultrahigh vacuum vessel of the Malmberg–Penning trap, and the 50 Ω coaxial cable from the trap flange up to the measuring device. The connection between the two parts is not matched and multiple reflections at the discontinuities occur. In order to characterize the transmission line a model has been built on a test bench and the results have been compared with the original signal to verify the initial assumption.

The test system, shown in Fig. 7, consisted in a 50 Ω coaxial cable (Coax1), connected by noncoaxial wires of length L_{12} to a kapton-insulated coaxial cable (Coax2) of impedance 18 Ω and length L_2. L_{12} and L_2 could be varied to match the experimentally detected signal. The antenna has been simulated with an open circuit of infinite impedance (the capacity of the antenna being included into that of the cable). The test has been performed with a time-domain reflectometric technique, i.e., generating an impulse of amplitude 1 V and duration 8 ns with a function generator and recording the line response. An example of the output is shown in Fig. 8, where we compare an experimental signal to the best-fitting results of the test bench system, obtained with the following parameters: $L_{12} = 0.16$ m, $Z_{12} = 300$ Ω, $L_2 = 1.10$ m, and $Z_2 = 18$ Ω. The comparison shows that the main features of the signal are well reproduced. Points (a), (b), and (c) indicate the presence of two discontinuities γ_1
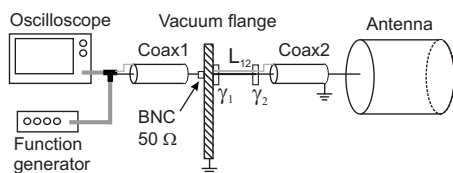

FIG. 7. Scheme of the signal acquisition line from the antenna reconstructed on a test bench. The discontinuities are indicated by γ_1 and γ_2.
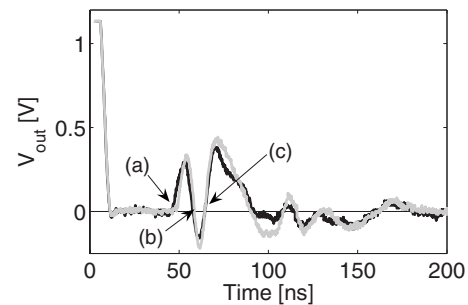

FIG. 8. Comparison between experimental (black line) and test bench (gray line) signals. The latter is the reflection signal obtained on a test bench with the reconstructed line and optimized parameters. The zero crossings (a), (b), and (c) indicate the presence of discontinuities.

and γ_2 and a third one due to the open termination of the line at the antenna. Successive zero crossings appear as a consequence of multiple reflections.

VI. TIME OF FLIGHT MEASUREMENT

The characterization of the transmission line helps in reconstructing the crossing of the traveling bunch through the trap. Since at low-energy the amplitude of the first peak of the electrostatic signal is small compared to residual noise oscillations, the front of the electron pulse cannot be deduced clearly from it. On the contrary, it is possible to infer this information from the second zero of the signal, directly connected to the presence of the line discontinuity. Further zeros are the result of signal superpositions due to multiple reflections in the transmission line and therefore no useful information can be drawn from them. We have used the second zero of the signal as input for the delay between the laser trigger and the crossing of the electron bunch. It is indeed clear from Fig. 6 that the position of this zero approaches the time origin as the bunch energy increases. The delay has been therefore extracted from the signal after denoising with the described technique.

This value has been converted into the effective time of flight (TOF) by adding the delay between bunch emission and trigger generation. This is calculated by estimating the TOF at 10 keV as the length-to-speed ratio (the total path from the photocathode to the antenna being 1807 mm) and amounts to an offset of 10.33 ns. The resulting TOF versus energy diagram, as seen in Fig. 9, shows that the values are in good agreement with the expected $E^{-1/2}$ trend. The error bars have been calculated using the rms value of the uncorrelated noise which affects the determination of the zero crossing position in time of the electrostatic signal. Since the slope of the signal around this zero crossing gets steeper, the TOF error bar is correspondingly reduced for increasing energies. With a maximum rms error of 2.1 ns measured at 2 keV bunch energy, we are still below the UV laser pulse duration. Therefore the TOF value can be used to verify the synchronization between the electron bunch and the IR laser which will be installed to perform Thomson backscattering.
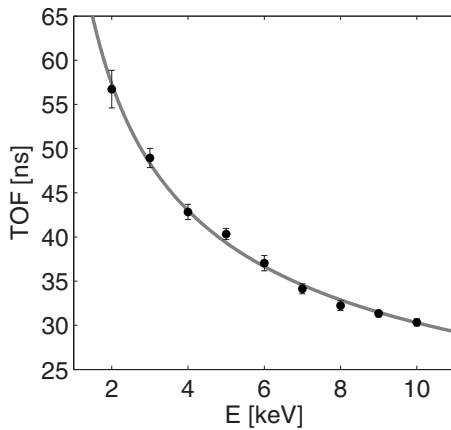
FIG. 9. TOF (full circles) deduced from the analysis of the denoised distorted signals are plotted vs the electron bunch energies. The continuous line is the $E^{-1/2}$ fit. Error bars represent the uncertainty coming from wavelet-filtered statistical noise.

VII. CONCLUSIONS AND OUTLOOK

A fast electrostatic diagnostic circuit and data postprocessing have been designed and successfully implemented in order to detect extremely weak and very low-SNR induced current signals in a Malmberg–Penning trap. With the proposed measurement system clear and significant signals can be detected with a bandwidth of approximately 100 MHz when 1–10 keV electron bunches travel through the pick-up electrodes. This has allowed the measurement of the pulses at different energies as well as an accurate estimate of the TOF, showing the consistency of the method. The information on the TOF will be needed for the Thomson backscattering diagnostics to guarantee the IR laser-bunch coincidence. In perspective, the results suggest that the electrostatic diag-

nostic technique can be advantageously exploited further for the nondestructive measurement of electron beam parameters such as length and radius. In this sense, more work has to be done to deduce from the electrostatic signal accurate and more detailed information on the electron bunches in different experimental conditions.

ACKNOWLEDGMENTS

[1] D. H. Dowell, S. Joly, A. Loulergue, J. P. de Brion, and G. Haouat, Phys. Plasmas **4**, 3369 (1997).
[2] R. C. Davidson and H. Qin, *Physics of Intense Charged Particle Beams in High Energy Accelerators* (Imperial College Press, London, 2001).
[3] L. Serafini and J. B. Rosenzweig, Phys. Rev. E **55**, 7565 (1997).
[4] D. Stratakis, R. A. Kishek, R. B. Fiorito, K. Tian, I. Haber, P. G. O'Shea, M. Reiser, and J. C. T. Thangaraj, Phys. Rev. ST Accel. Beams **12**, 020101 (2009).
[5] J. H. Malmberg and J. S. deGrassie, Phys. Rev. Lett. **35**, 577 (1975).
[6] M. Amoretti, G. Bettega, F. Cavaliere, M. Cavenago, F. De Luca, R. Pozzoli, and M. Romé, Rev. Sci. Instrum. **74**, 3991 (2003).
[7] G. Bettega, F. Cavaliere, A. Illiberi, R. Pozzoli, M. Romé, M. Cavenago, and Yu. Tsidulko, Appl. Phys. Lett. **84**, 3807 (2004).
[8] B. Paroli, G. Bettega, F. Cavaliere, F. De Luca, G. Maero, R. Pozzoli, M. Romé, M. Cavenago, and C. Svelto, J. Phys. D **42**, 175203 (2009).
[9] S. Ramo, Proc. IRE **27**, 584 (1939).
[10] J. Millman and A. Grabel, *Microelectronics* (McGraw-Hill, New York, 1987).
[11] G. Bettega, B. Paroli, R. Pozzoli, M. Romé, and C. Svelto, Meas. Sci. Technol. **19**, 085703 (2008).
[12] R. C. Davidson, *An Introduction to the Physics of Nonneutral Plasmas* (Addison-Wesley, Redwood City, 1990).
[13] A. Grossmann and J. Morlet, SIAM J. Math. Anal. **15**, 723 (1984).
[14] D. L. Donoho and I. M. Johnstone, Biometrika **81**, 425 (1994).
[15] D. L. Donoho, IEEE Trans. Inf. Theory **41**, 613 (1995).